

**1 Impact of velocity correlation and distribution on**  
**2 transport in fractured media: field evidence and**  
**3 theoretical model**

Peter K. Kang<sup>1</sup>, Tanguy Le Borgne<sup>2</sup>, Marco Dentz<sup>3</sup>, Olivier Bour<sup>2</sup>, and

Ruben Juanes<sup>1</sup>

---

Corresponding author: T. Le Borgne, Université de Rennes 1, CNRS, Geosciences Rennes,  
UMR 6118, Rennes, France. (tanguy.le-borgne@univ-rennes1.fr)

<sup>1</sup>Massachusetts Institute of Technology,  
77 Massachusetts Avenue, Cambridge,  
Massachusetts 02139, USA

<sup>2</sup>Université de Rennes 1, CNRS,  
Geosciences Rennes, UMR 6118, Rennes,  
France

<sup>3</sup>Institute of Environmental Assessment  
and Water Research (IDAEA), Spanish  
National Research Council (CSIC), 08034  
Barcelona, Spain

**Abstract.** Flow and transport through fractured geologic media often leads to anomalous (non-Fickian) transport behavior, the origin of which remains a matter of debate: whether it arises from variability in fracture permeability (velocity distribution), connectedness in the flow paths through fractures (velocity correlation), or interaction between fractures and matrix. Here we show that this uncertainty of distribution- vs. correlation-controlled transport can be resolved by combining convergent and push-pull tracer tests because flow reversibility is strongly dependent on velocity correlation, whereas late-time scaling of breakthrough curves is mainly controlled by velocity distribution. We build on this insight, and propose a Lagrangian statistical model that takes the form of a continuous time random walk (CTRW) with correlated particle velocities. In this framework, velocity distribution and velocity correlation are quantified by a Markov process of particle transition times that is characterized by a distribution function and a transition probability. Our transport model accurately captures the anomalous behavior in the breakthrough curves for both push-pull and convergent flow geometries, with the same set of parameters. Thus, the proposed correlated CTRW modeling approach provides a simple yet powerful framework for characterizing the impact of velocity distribution and correlation on transport in fractured media.

## 1. Introduction

Understanding flow and transport through fractured geologic media is essential for improving forecasts, management and risk assessment of many subsurface technologies, including geologic nuclear waste disposal [Bodvarsson *et al.*, 1999], geologic CO<sub>2</sub> storage [Szulczewski *et al.*, 2012], oil and gas production from fractured reservoirs [Kazemi *et al.*, 1976], enhanced geothermal systems [Pruess, 2006], shale-gas development [Curtis, 2002; Cueto-Felgueroso and Juanes, 2013], and groundwater contamination and remediation [Gerke and van Genuchten, 1993; Huyakorn *et al.*, 1994]. Moreover, if we conceptualize fractured geologic media as a network system, this knowledge can have implications to other physical processes, including disease spreading through river networks [Rinaldo *et al.*, 2012] and the air transportation system [Nicolaidis *et al.*, 2012], urban traffic [Kerner, 1998], and nutrient transport through preferential paths in biofilms [Wilking *et al.*, 2013].

There are two main sources of uncertainty for transport through fractured media: uncertainty in the fracture geometrical properties, including fracture aperture, roughness, location and connectivity describing fracture geometry [Tsang *et al.*, 1988; Cacas *et al.*, 1990; Méheust and Schmittbuhl, 2000; de Dreuzy *et al.*, 2001]; and uncertainty in the physical transport processes impacting the flow and transport such as advection, diffusion, dispersion and adsorption [Neretnieks, 1983; Haggerty and Gorelick, 1995; Becker and Shapiro, 2003]. The fracture geometrical properties and the physical transport processes are interdependent, and may lead to anomalous transport. Anomalous transport, understood as the nonlinear scaling with time of the mean square displacement of trans-

ported particles, is a characteristic feature of transport through porous and fractured geologic media [Berkowitz *et al.*, 2006; Bijeljic and Blunt, 2006; Berkowitz and Scher, 1997].

Fracture geometrical properties impact macroscopic transport by controlling the velocity distribution at multiple scales. Fracture roughness leads to a broad velocity probability density function (PDF) at the fracture scale, and the variability in fracture aperture between fracture planes leads to a broad velocity PDF at the network scale [Nordqvist *et al.*, 1992; Brown *et al.*, 1998; Méheust and Schmittbuhl, 2000]. In the following, we will refer to PDF as “probability distribution” or simply “distribution”. In addition, fracture length impacts velocity correlation, since the velocity within each fracture is usually highly correlated. Therefore, the fracture geometrical properties impact both the transport velocity distribution and velocity correlation. In practice, however, the fracture geometrical information is very limited and only a few dominant properties, such as relative fracture aperture and dominant major fractures, are identifiable [Dorn *et al.*, 2012].

Heterogeneous advection, matrix diffusion, hydrodynamic dispersion and adsorption are four physical transport mechanisms that impact transport of nonreactive tracers through fractured media. Heterogeneous advection, which results from the separation of mass into different flow channels, can be partially reversible when the flow field is reversed. Matrix diffusion is a diffusive mass exchange between fractures and the surrounding rock matrix, which is not a time-reversible process. Hydrodynamic dispersion describes tracer spreading due to the combined effect of pore-fluid diffusion and local velocity heterogeneity within the fracture. Adsorption refers to the adhesion of dissolved tracers to solid

surfaces. All these physical phenomena can be understood as either an advective or a diffusive process. Heterogeneous advection is an advective process, and matrix diffusion, hydrodynamic dispersion, and adsorption can be understood as diffusive processes. The competition between advective and diffusive processes is therefore manifested by the reversibility of flow, which in turn is controlled by velocity correlation. Advection is a time-reversible process: when flow is reversed, the spreading caused by heterogeneous advection collapses back. In contrast, diffusion is a time-irreversible process: particle spreading cannot be collapsed by reversing the flow. The advective versus diffusive-controlled breakthrough curve tailing has been tested by using tracers of different diffusivity and difference pumping rates [Moench, 1995; Becker and Shapiro, 2000; Reimus and Callahan, 2007]. These physical transport mechanisms also impact the Lagrangian velocity distribution. For example, heterogeneous advection induces a broad velocity distribution via the combination of slow paths and fast paths, matrix diffusion via the trapping of tracers in the rock matrix, and adsorption via the adhesion of particles onto the rock surface.

In summary, the complex interplay between fracture geometrical properties and physical transport processes determines the average particle transport behavior via velocity distribution and velocity correlation. Recent studies have shown that tracer transport through fractured and porous media is strongly modulated by the particle velocity distribution and velocity correlation [Le Borgne *et al.*, 2008; Kang *et al.*, 2011a; de Anna *et al.*, 2013; Kang *et al.*, 2014]. Here, we develop a stochastic model of transport that recognizes the impact of both velocity distribution and velocity correlation as an integral part of its ability to make predictions of transport at the field scale.

## 2. Field experiments

A signature of anomalous transport in the field is the late-time tailing of breakthrough curves (BTCs), that is, time series of tracer concentration at the pumping well. Breakthrough curves are affected by both the underlying fracture geometrical properties and the physical transport processes such as advection, diffusion, dispersion and adsorption. Thus, they are sensitive to both velocity distribution and velocity correlation.

We build on the seminal observation by *Tsang* [1995], who suggested that the combination of different tracer tests could be used to reduce the uncertainty in the characterization of fractured media. Here, we propose a framework to combine single-well (push-pull) and two-well (convergent) tests to extract transport parameters.

### 2.1. Field site and tracer-test setup

We conducted a series of field tracer tests under forced hydraulic gradient in a saturated fractured granite formation at the Ploemeur observatory (H+ network) [*de Dreuzay et al.*, 2006; *Ruelleu et al.*, 2010] (Figure 1). Geologically, the site is located at the contact between the underlying fractured granite and the overlying mica schist. The matrix permeability of granite is extremely low and, therefore, groundwater flows mainly through the network of fractures.

For this study, we used two boreholes, B1 (83 m deep) and B2 (100 m deep), which are 6 m apart. Previous work [*Le Borgne et al.*, 2007; *Dorn et al.*, 2012, 2013] has identified four major conductive fractures intersecting B1, labelled B1-1 (24 m deep), B1-2 (50 m), B1-3 (63 m) and B1-4 (79 m), and four major conductive fractures intersecting B2, labelled B2-2 (56 m), B2-3 (59 m), B2-4 (79 m) and B2-5 (97 m). We designed and conducted convergent and push-pull tests at two different fractures: B1-2 and B1-4. Regional flow

may influence the reversibility of the flow [*Lessoﬀ and Konikow*, 1997; *Altman et al.*, 2002]. Direct measurements of ambient flow were obtained at the experimental site using the finite volume point dilution method using packers to isolate the fractures where the tracer tests were performed [*Brouyère et al.*, 2008]. The ambient flow measured in B1-2 fracture was found to be below the detection limit ( $10^{-7}$  m<sup>3</sup>/s), while that measured in B1-4 was about  $10^{-6}$  m<sup>3</sup>/s. Although these are local estimates, this suggests that ambient flow is too small ( $\leq 0.06$  L/m) to affect flow field generated by the injection/withdrawal rates (5 to 6 L/m). As a tracer, we used fluorescein, which is widely used for groundwater tracing and known to be non-reactive, insensitive to pH and salinity, and moderately resistant to adsorption and photochemical bleaching [*Smart and Laidlaw*, 1977].

#### 2.1.1. Convergent tracer test

In the convergent test, we inject a known mass of tracer into an injection borehole (B1) and measure the tracer concentration at the pumping borehole (B2) (Fig. 2(a,b,c)). To place the tracer at the target fracture, we installed a double-packer at the injection borehole at two different depths, targeting the B1-2 and B1-4 fractures in separate experiments. To form a stationary, radial convergent flow configuration, a constant pumping rate was established at borehole B2 throughout the experiment. Once a stationary pressure field is achieved, we inject the tracer at borehole B1 for a short duration compared to the total duration of the experiment, and at a small injection rate ( $<1\%$  of the pumping rate at B2). When the injection of tracer is completed, we recirculate the fluid inside the double-packer system to prevent the possible remaining tracer from continuing to leak into the formation. We have monitored the well concentration during the experiment

and confirmed the tracer concentration was small enough during the early stage of the experiment.

### 2.1.2. Push-pull tracer test

In the push-pull test, we first inject a known mass of tracer into borehole B1, and continue to inject fresh water for a fixed duration of time (“push” phase). We then reverse the flow and pump water from the same borehole with the same flow rate (“pull” phase), and measure the arrival tracer concentration (Fig. 2(d,e,f)). Again, a double-packer system was installed to isolate the injection into the desired fracture plane.

## 2.2. Field test results

Additional details on the conditions and parameters of the field experiments are given in Table 1, and the measured BTCs are shown in Figure 3. As expected, the BTCs are broader for the convergent tests than for the push-pull tests, given that in the latter the spreading during the “push” phase is partially recovered during the “pull” phase. Indeed, the degree to which the initial tracer spreading is reversed is an indication of the strength of velocity correlation.

Analyzing the two convergent tests, we note that the power-law late-time scalings are different, exhibiting a slope of  $\sim 1.75$  for B1-2 and  $\sim 1.85$  for B1-4. This difference reflects different velocity distributions, and can be interpreted as different levels of heterogeneity. The gentler slopes in the BTCs indicate a broader range (higher probability) towards small velocities.

Motivated by these field observations, we review existing theoretical transport models, and develop a new model that takes into account both velocity distribution and velocity correlation.



### 3. Existing models of transport

Various approaches have been proposed to model flow and transport through fractured media, ranging from equivalent porous medium approaches that represent the fractured medium as a single continuum [Neuman *et al.*, 1987; Tsang *et al.*, 1996], to discrete fracture networks that explicitly represent fractures as entities embedded in the surrounding matrix [Kiraly, 1979; Cacas *et al.*, 1990; Moreno and Neretnieks, 1993; Juanes *et al.*, 2002; Molinero *et al.*, 2002; Karimi-Fard *et al.*, 2004; Martinez-Landa and Carrera, 2005; Molinero and Samper, 2006; Martinez-Landa *et al.*, 2012; de Dreuzy *et al.*, 2012a; Schmid *et al.*, 2013]. Dual porosity models are, in some sense, in between these two extremes, and conceptualize the fractured-porous medium as two overlapping continua, which interact via an exchange term [Bibby, 1981; Feenstra *et al.*, 1985; Maloszewski and Zuber, 1985; Gerke and van Genuchten, 1993].

Stochastic models that account for the observed non-Fickian global transport behavior in fractured media include continuous-time random walks (CTRW) [Berkowitz and Scher, 1997; Geiger *et al.*, 2010; Kang *et al.*, 2011b, a], fractional advection-dispersion equations (fADE) [Benson *et al.*, 2000], multirate mass transfer (MRMT) [Haggerty and Gorelick, 1995; Carrera *et al.*, 1998; Le Borgne and Gouze, 2008], stochastic convective stream tube (SCST) models [Becker and Shapiro, 2003], and Boltzmann equation approaches [Benke and Painter, 2003]. All of these models are valid under their own assumptions, and have played an important role in advancing the understanding of transport through fractured media. Among these models, the MRMT and SCST approaches have been applied to model non-Fickian tracer transport in both push-pull and convergent tests at the same site [Haggerty *et al.*, 2001; McKenna *et al.*, 2001; Becker and Shapiro, 2003].

Below, we briefly revisit the basic formulations of the classical advection-dispersion, stochastic-convective streamtube and multirate mass transfer models for radial flow geometries, and discuss their ability to capture BTCs for convergent and push-pull tests.

### 3.1. Advection-dispersion equation (ADE) model

The classical advection-dispersion equation (ADE) in radial coordinates is given by

$$\frac{\partial c(r, t)}{\partial t} + \frac{k_v}{r} \frac{\partial c(r, t)}{\partial r} - \frac{\alpha k_v}{r} \frac{\partial^2 c(r, t)}{\partial r^2} = 0, \quad (1)$$

where  $\alpha$  is dispersivity and  $k_v = Q/(2\pi b_{\text{eff}})$  with  $Q$  the volumetric flow rate and  $b_{\text{eff}}$  the mass balance aperture. The mass balance aperture,  $b_{\text{eff}}$ , can be defined as  $Q\langle\tau_a\rangle/(\pi([r(0) + r_c]^2 - r(0)^2))$  for a convergent tracer test, where  $\langle\tau_a\rangle$  is the mean solute arrival time,  $r(0)$  is the pumping point, and  $r_c$  the distance between the tracer injection point and the withdrawal point [Tsang, 1992]. The mass balance aperture,  $b_{\text{eff}}$ , represents an average aperture along the flow paths for tracer transport. Since we will use a Lagrangian modeling approach in the following, we formulate the advection-dispersion model in terms of radial particle trajectories. This can be done by rewriting (1) in terms of a conserved variable in radial coordinates,

$$p(r, t) = 2\pi b_{\text{eff}} r c(r, t), \quad (2)$$

which is the particle density per unit radial length. Inserting the latter into (1) we obtain

$$\frac{\partial p(r, t)}{\partial t} + \frac{\partial}{\partial r} \frac{k_v}{r} p(r, t) - \frac{\partial^2}{\partial r^2} \frac{\alpha k_v}{r} p(r, t) = 0. \quad (3)$$

The equivalent Langevin equation is given by

$$\frac{dr(t)}{dt} = \frac{k_v}{r(t)} + \sqrt{\frac{2\alpha k_v}{r(t)}} \xi_r(t), \quad (4)$$

where  $\xi_r(t)$  is a Gaussian white noise of zero mean and unit variance. Here and in the following, we employ the Ito interpretation of the Langevin equation (4) [Risken, 1989]. The particle density is given in terms of the radial trajectories as  $p(r, t) = \langle \delta[r - r(t)] \rangle$ , and by virtue of (2), we obtain for the concentration distribution

$$c(r, t) = \frac{1}{2\pi b_{\text{eff}} r} \langle \delta[r - r(t)] \rangle. \quad (5)$$

The angular brackets  $\langle \cdot \rangle$  denote the average over all solute particles.

The solute breakthrough curve at a distance  $r_c$  from the injection point  $r(0)$  is given in terms of the probability density function of the particles' first arrival times at the radius  $r = r(0) + r_c$ ,

$$\tau_a = \inf \{t \mid |r(t) - r(0)| \geq r_c\}, \quad (6)$$

which is defined by

$$f(\tau) = \langle \delta(\tau - \tau_a) \rangle. \quad (7)$$

The mean solute arrival time at a radius  $r_c$  is given by

$$\langle \tau_a \rangle = \frac{[r(0) + r_c]^2 - r(0)^2}{2k_v}, \quad (8)$$

which is also the peak arrival time.

### 3.2. Stochastic convective stream tube (SCST) model

Stochastic convective streamtube models assume that transport occurs along independent streamtubes. Transport within streamtubes is one-dimensional, and there is no mass exchange between individual streamtubes [Dagan and Bressler, 1979; Cirpka and Kitandis, 2000; Ginn, 2001; Becker and Shapiro, 2003]. Thus, these models are sometimes called minimum mixing models. For uniform mean flow, transport in a single radial streamtube of type  $\omega$  is given by [Ginn, 2001; Becker and Shapiro, 2003]

$$\frac{\partial c_\omega(x, t)}{\partial t} + \frac{k_\omega}{r} \frac{\partial c_\omega(r, t)}{\partial r} - \frac{\alpha k_\omega}{r} \frac{\partial^2 c_\omega(r, t)}{\partial r^2} = 0, \quad (9)$$

where  $k_\omega$  is given by  $k_\omega = Q_\omega / (2\pi b_\omega \phi_\omega)$  with  $Q_\omega$  the flow rate,  $b_\omega$  the typical aperture and  $\phi_\omega$  the porosity of the streamtube, and  $\alpha$  is the dispersivity. The total solute concentration  $c(r, t)$  is given by the average of  $c_\omega(r, t)$  over all streamtubes

$$c(r, t) = \int d\omega \mathcal{P}(\omega) c_\omega(r, t), \quad (10)$$

where  $\mathcal{P}(\omega)$  denotes the PDF of streamtubes. Macroscopic solute dispersion here is caused predominantly by velocity contrasts between streamtubes. Transport is fully reversible for  $\alpha = 0$ . The only irreversible transport mechanism in this framework is dispersion along the streamtubes.

The Lagrangian formulation of transport in a single streamtube  $\omega$  is identical to (4) because transport along a streamtube is given by the radial advection-dispersion equation (9). In many realistic flow and transport scenarios, radial dispersion can be dis-

219 regarded because its effect on solute spreading is negligible compared with advective  
 220 heterogeneity. For  $\alpha = 0$ , the Langevin equation (4) for a single streamtube  $\omega$  reduces to

$$\frac{dr_\omega(t)}{dt} = \frac{k_\omega}{r_\omega(t)}. \quad (11)$$

221 Consequently, in the case of an instantaneous solute injection, and using (5), we obtain  
 222 the following expression for the total solute concentration (10),

$$c(r, t) = \frac{1}{2\pi br} \int d\omega \mathcal{P}(\omega) \phi_\omega^{-1} \delta[r - r_\omega(t)]. \quad (12)$$

223 The solute arrival time  $\tau_\omega$  at a distance  $r_c$  in a single streamtube is given by

$$\tau_\omega = \frac{[r_c + r(0)]^2 - r(0)^2}{2k_\omega}. \quad (13)$$

224 The total solute breakthrough is given by averaging the deterministic arrival times  $\tau_\omega$  over  
 225 the ensemble of streamtubes, which is characterized by the distribution  $\mathcal{P}_{k_\omega}(k)$  of  $k_\omega$ ,

$$f(\tau) = \int dk \mathcal{P}_{k_\omega}(k) \delta[\tau - \tau_\omega(k)]. \quad (14)$$

226 For a push-pull tracer test, we immediately see that the breakthrough curve is given by  
 227  $f(\tau) = \delta(\tau - 2t_p)$ , where  $t_p$  is the push time. The solute arrival time at the injection point  
 228 is simply twice the push time because of the full reversibility of transport, as described  
 229 by (11).

### 3.3. Multirate mass transfer (MRMT) model

The MRMT model considers solute transport under mass transfer between a single mobile zone and a series of immobile zones. Fast solute transport in the mobile zone and solute retardation in the immobile zones can lead to non-Fickian spatial distributions and breakthrough curves, and in general to an increase of solute dispersion. Solute mass conservation in the mobile domain is expressed in radial coordinates by

$$\phi_m \frac{\partial c_m(r, t)}{\partial t} + \frac{\phi_m k_v}{r} \frac{\partial c_m(r, t)}{\partial r} - \frac{\alpha \phi_m k_v}{r} \frac{\partial^2 c_m(r, t)}{\partial r^2} = -\phi_{im} \frac{\partial c_{im}(r, t)}{\partial t} \quad (15)$$

where  $\phi_m$  and  $\phi_{im}$  are the (average) porosities of the mobile and immobile continua, respectively,  $k_v = Q/(2\pi b\phi_m)$  with  $Q$  the flow rate and  $b$  the width of the injection interval, and  $\alpha$  is the dispersivity. Mass transfer between the mobile and immobile regions is linear and thus, assuming zero initial conditions in the immobile regions, the mobile  $c_m(r, t)$  and immobile  $c_{im}(r, t)$  solute concentrations are related by [Dentz and Berkowitz, 2003]

$$c_{im}(r, t) = \int_0^t dt' \varphi(t - t') c_m(r, t'), \quad (16)$$

where  $\varphi(t)$  is the memory function that encodes the specific mass transfer mechanism [Haggerty and Gorelick, 1995; Harvey and Gorelick, 1995; Carrera et al., 1998; Dentz and Berkowitz, 2003; Dentz et al., 2011a]. For linear first-order mass exchange,  $\varphi(t)$  determines the distribution of transfer rates between mobile and immobile regions [Haggerty and Gorelick, 1995]. For diffusive mass transfer, it encodes the geometries and the characteristic diffusion scales of the immobile regions [Dentz et al., 2011a]. Combining (15) and (16), we write the temporally non-local single-equation MRMT model

$$\begin{aligned}
& \phi_m \frac{\partial c_m(r, t)}{\partial t} + \phi_{im} \frac{\partial}{\partial t} \int_0^t dt' \varphi(t - t') c_m(r, t') \\
& + \frac{\phi_m k_v}{r} \frac{\partial c_m(r, t)}{\partial r} - \frac{\alpha \phi_m k_v}{r} \frac{\partial^2 c_m(r, t)}{\partial r^2} = 0.
\end{aligned} \tag{17}$$

247 It has been shown that the MRMT model is equivalent to CTRW models characterized  
 248 by uncoupled transition length and time distributions, and to time fractional advection-  
 249 dispersion models [*Dentz and Berkowitz, 2003; Schumer et al., 2003; Benson and Meer-*  
 250 *schaert, 2009*]. The MRMT model was employed by *Haggerty et al. [2001]* to interpret  
 251 breakthrough curves for radial push-pull tracer tests in fractured dolomite. *Le Borgne*  
 252 *and Gouze [2008]* used a CTRW implementation of MRMT to simulate breakthrough  
 253 curves for radial push-pull tracer tests. The MRMT models and its equivalent CTRW  
 254 and fADE formulations describe solute dispersion as an irreversible process. In these mod-  
 255 eling frameworks, retardation events that essentially cause macroscopic solute dispersion  
 256 are independent. Thus, transport is irreversible upon flow reversal.

257 As in the previous section, we formulate the radial MRMT model (17) in a Lagrangian  
 258 framework. Following the approach employed in *Le Borgne and Gouze [2008]*, we imple-  
 259 ment MRMT in terms of the continuous time random walk

$$r_{n+1} = r_n + \frac{k_v}{r_n} \Delta s + \sqrt{\frac{2\alpha k_v \Delta s}{r_n}} \xi_n, \tag{18a}$$

$$t_{n+1} = t_n + \Delta s + \eta_n \Delta s, \tag{18b}$$

260 where the  $\xi_n$  are identical independently distributed Gaussian random variables with zero  
 261 mean and unit variance, and  $\Delta s$  is an operational time increment. The dimensionless  
 262 random time increments  $\eta_n$  are identical independently distributed random variables with

the distribution density  $\psi(\eta)$ . For  $\eta_n \equiv 0$ , the system (18) is identical to the discretized version of (4) in the Ito interpretation.

The continuous time random walk (18) is equivalent to (17) in the limit of small  $\Delta s$  with the identification [Dentz and Berkowitz, 2003]

$$\varphi(t) = \frac{\phi_m}{\phi_{im}} \mathcal{L}^{-1} \left\{ \frac{1 - \psi^*(\lambda \Delta s)(1 + \lambda \Delta s)}{\lambda \Delta s \psi^*(\lambda \Delta s)} \right\}, \quad (19)$$

where  $\mathcal{L}^{-1}\{\cdot\}$  denotes the inverse Laplace transform,  $\psi^*(\lambda)$  is the Laplace transform of  $\psi(t)$ , and  $\lambda$  the Laplace variable. Here and in the following, Laplace-transformed quantities are marked by an asterisk.

The distribution of solute arrival times for both convergent and push-pull tracer tests is obtained from the individual particle arrival times  $\tau_a = \inf(t_n | |r_n - r_0| > r_c)$  as

$$f(\tau) = \overline{\delta(\tau - \tau_a)}, \quad (20)$$

where the overbar  $\overline{(\cdot)}$  denotes the average over the ensemble of all particles characterized by the stochastic series of dimensionless retention times  $\{\eta_n\}$ . Notice that the arrival time distribution in the push-pull case does not reduce to a delta-density, as in the SCST model. Solute transport is irreversible in the MRMT approach that we presented.

### 3.4. Comparison of ADE, SCST and MRMT models

The traditional ADE formulation presented in section 3.1 does not have the ability to capture anomalous transport, manifested as a power-law tailing in BTCs. To overcome this limitation, SCST and MRMT models have been applied to explain BTCs for convergent and push-pull tests. To show the fundamental difference between the two models,



we run both convergent and push-pull simulation with the two models. For the MRMT model, we employ the Pareto waiting time distribution

$$\psi(\eta) = \frac{\beta}{\eta_0} \left( \frac{\eta}{\eta_0} \right)^{-1-\beta}, \quad \eta > \eta_0, \quad (21)$$

with  $0 < \beta < 2$ . For the distribution of the  $k_\omega$  in the SCST approach we employ the distribution

$$\mathcal{P}_{k_\omega}(k) = \frac{\beta}{k_0} \left( \frac{k}{k_0} \right)^{\beta-1}, \quad k < k_0. \quad (22)$$

The distributions (21) and (22) for the MRMT and SCST models, respectively, give identical slopes for the long time behavior of the BTCs in the convergent tracer tests. In Figure 4, we show the modeling results for MRMT and SCST models. We can see the clear distinction between the two models. Since MRMT does not have a mechanism to capture the reversibility of advective spreading, the BTCs of convergent and push-pull tests are almost identical. In contrast, the stream tube model assumes perfect correlation in velocity, and we observe perfect reversibility in the BTC for the push-pull tracer test in the absence of local dispersion within streamtubes. In reality, there always exists both irreversible diffusive and reversible advective processes, and our objective is to develop a stochastic model that recognizes the competition between the two processes.

The limitations of MRMT and SCST (as well as ADE and classical CTRW) in reproducing the time-reversibility behavior of both types of tracer tests could be relieved if the models were applied in multidimensions, with spatially variable permeability fields. This, however, would rapidly increase model complexity, the number of model parameters, and

would require more field data to reliably constrain those parameters. The objective of our work is to propose a parsimonious theoretical model that accounts for reversible and irreversible processes in 1D radial coordinates.

#### 4. Continuous time random walks (CTRW) with correlated velocities

As discussed in Section 3.4, the SCST and MRMT frameworks represent transport models that exhibit full reversibility and complete irreversibility, respectively. The breakthrough curves obtained from convergent and push-pull tracer tests at the Ploemeur fractured aquifer, however, exhibit neither full reversibility nor complete irreversibility (Figure 3). Here we develop a stochastic model based on a correlated CTRW approach [Le Borgne et al., 2008; Kang et al., 2011a; de Anna et al., 2013; Kang et al., 2014], with the following two design criteria: Lagrangian velocity correlation that captures flow reversibility, and particle velocity distribution that captures velocity heterogeneity.

##### 4.1. Model formulation

The starting point for the model is the Langevin equation (4) in differential form

$$dr(t) = \frac{k_v dt}{r(t)} + \sqrt{2\alpha \frac{k_v dt}{r(t)}} \xi_r(t). \quad (23)$$

By defining the differential space increment  $d\vartheta = k_v dt / r(t)$  [Dentz et al., 2009; Dentz and Bolster, 2010], equation (23) transforms into

$$dr(\vartheta) = d\vartheta + \sqrt{2\alpha d\vartheta} \xi_r(\vartheta), \quad (24a)$$

$$dt(\vartheta) = \frac{r(\vartheta)}{k_v} d\vartheta. \quad (24b)$$

Discretizing this system in  $\vartheta$  and setting  $\Delta\vartheta = \ell$  gives the following system of equations for the particle trajectories in space and time coordinates, or in other words, a CTRW,

$$r_{n+1} = r_n + \ell + \sqrt{2\alpha\ell}\xi_n, \quad (25a)$$

$$t_{n+1} = t_n + \frac{\ell r_n}{k_v}. \quad (25b)$$

Notice that this CTRW is characterized by a radially dependent time increment. It is by definition equivalent to (3) in the limit of small  $\ell \ll L$ , with  $L$  a macroscopic observation scale.

We generalize this CTRW heuristically in order to account for variability in radial particle velocities that may be induced by spatial variability in hydraulic conductivity and retardation properties of the medium. Notice that the transport velocity depends on both hydraulic conductivity and porosity. *Le Borgne et al.* [2008] and *Kang et al.* [2011a] demonstrated that the impact of flow heterogeneity on large scale solute transport can be quantified in terms of CTRWs whose time increments form a Markov chain based on the observation that the series of Lagrangian particle velocities form a Markov process.

We define here a radial correlated CTRW that allows to vary the velocity correlation (persistence of particle velocities) and velocity distribution (PDF of particle velocities), to represent and quantify both correlation and distribution-induced anomalous transport features, and to discriminate between them [*Dentz and Bolster*, 2010]. Thus, we generalize the stochastic process (25b) of particle times according to

$$t_{n+1} = t_n + \frac{\ell r_n}{k_v}\eta_n, \quad (25c)$$

where the dimensionless time increments  $\{\eta_n\}$  form a Markov chain characterized by the marginal distribution density  $\psi_0(\eta)$  of initial increments  $\eta_0$  and the one-step transition probability density  $\psi_1(\eta|\eta')$ . The Chapman-Kolmogorov equation for the  $n$ -step transition time density  $\psi_n(\eta|\eta')$  reads

$$\psi_n(\eta|\eta') = \int_0^\infty d\eta'' \psi_{n-m}(\eta|\eta'') \psi_m(\eta''|\eta'). \quad (26)$$

The density  $\psi_n(\eta)$  of random increments  $\eta_n$  after  $n$  steps is given by

$$\psi_n(\eta) = \int_0^\infty d\eta' \psi_n(\eta|\eta') \psi_0(\eta'). \quad (27)$$

We set here  $\psi_0(\eta) = \psi(\eta)$  equal to the steady state density, which is an eigenfunction of the transition density  $\psi_1(\eta|\eta')$  and therefore  $\psi_n(\eta) = \psi(\eta)$ . This is equivalent to assuming that particles sample velocities from the steady state Lagrangian velocity distribution from the beginning. Equations (25a) and (25c) constitute the equations of motion of solute particles in the proposed radial correlated CTRW approach, where  $\psi(\eta)$  determines the velocity distribution and  $\psi_1(\eta|\eta')$  determines the velocity correlation.

## 4.2. Limiting cases

In the following, we briefly determine the limits of the system (25a) and (25c) for fully correlated and fully uncorrelated dimensionless time increments  $\{\eta_n\}$ .

### 4.2.1. Fully correlated case

In the limit of fully correlated  $\{\eta_n\}$ , i.e.,  $\psi_1(\eta|\eta') = \delta(\eta - \eta')$ , where  $\delta$  denotes the Kronecker delta, equations (25a) and (25c) reduce to

$$r_{n+1} = r_n + \ell + \sqrt{2\alpha\ell}\xi_n, \quad (28a)$$

$$t_{n+1} = t_n + \frac{\ell r_n}{k_\omega}, \quad (28b)$$

where we defined the constant  $k_\omega = k_v/\eta_\omega$  with  $\eta_\omega$  the perfectly persistent increment, which is distributed according to  $\psi(\eta)$ . Each  $\eta_\omega$ , or  $k_\omega$ , represents a streamtube in the sense of the SCST model. In fact, just as (25a) and (25b) are equivalent to (3), so is system (28), which constitutes the equivalence of (28) and (9). Therefore, the fully correlated case of the proposed model is equivalent to the SCST model.

#### 4.2.2. Fully uncorrelated case

In the limit of fully uncorrelated  $\{\eta_n\}$ , i.e.,  $\psi_1(\eta|\eta') = \psi(\eta)$ , the system (25a) and (25b) is equivalent to the following non-local radial advection dispersion equation

$$\frac{\partial c(r, t)}{\partial t} + \int_0^t dt' \left[ \frac{\phi k_v}{r} \frac{\partial}{\partial r} M(r, t - t') c(r, t') - \frac{\alpha \phi k_v}{r} \frac{\partial^2}{\partial r^2} M(r, t - t') c(r, t') \right] = 0, \quad (29)$$

with the radially dependent memory function

$$M(r, t) = \mathcal{L}^{-1} \left\{ \frac{\lambda \eta_k(r) \psi^*[\lambda \eta_k(r)]}{1 - \psi^*[\lambda \eta_k(r)]} \right\}. \quad (30)$$

We defined  $\eta_k(r) = \ell r/k_v$  for compactness. The memory function depends explicitly on the radial position through the radially dependent time scale  $\eta_k(r)$ . Notice that this radial CTRW model is in general different from the radial MRMT model (17).

### 4.3. Model implementation

The proposed CTRW with correlated transition times (25a) and (25c) is solved using random walk particle tracking. The model has three key transport characteristics: the probability distribution of the dimensionless time increments,  $\psi(\eta)$ , the one step transition probability that quantifies the velocity correlation,  $\psi_1(\eta|\eta')$ , and the local dispersivity,  $\alpha$ . Here we present how to characterize  $\psi(\eta)$  and  $\psi_1(\eta|\eta')$ , and explain in detail the random walk particle tracking algorithm used to solve for the BTCs in the convergent and push-pull scenarios.

#### 4.3.1. Transition probability and correlation

To independently control velocity distribution and velocity correlation, we describe the Markov process  $\{\eta_n\}$  with the steady state distribution,  $\psi(\eta)$ . The continuous non-dimensional transition times  $\eta$  are discretized into  $N$  classes,  $\eta \in \bigcup_{j=1}^N (\eta_j, \eta_{j+1}]$ , such that the transition probabilities between the classes are represented by the  $N \times N$  transition matrix  $\mathbf{T}$ , with components

$$T_{ij} = \int_{\eta_i}^{\eta_{i+1}} d\eta \int_{\eta_j}^{\eta_{j+1}} d\eta' \psi_1(\eta|\eta') \psi(\eta') / \int_{\eta_j}^{\eta_{j+1}} d\eta' \psi(\eta'). \quad (31)$$

The transition matrix satisfies  $\mathbf{T}^{n+m} = \mathbf{T}^n \mathbf{T}^m$ . Here, we choose equiprobable binning such that

$$\int_{\eta_i}^{\eta_{i+1}} d\eta \psi(\eta) = \frac{1}{N}. \quad (32)$$

With this condition,  $\mathbf{T}$  is a doubly stochastic matrix, which therefore satisfies

$$\sum_{i=1}^N T_{ij} = \sum_{j=1}^N T_{ij} = 1. \quad (33)$$

For a large number of transitions, the transition matrix converges towards the uniform matrix,

$$\left[ \lim_{n \rightarrow \infty} \mathbf{T}^n \right]_{ij} = \frac{1}{N}, \quad (34)$$

whose eigenvalues are 1 and 0. Thus, correlation can be measured by the convergence of  $\mathbf{T}$  towards the uniform matrix. The correlation length is determined by the decay rate of the second largest eigenvalue  $\chi_2$  (the largest eigenvalue of a stochastic matrix is always 1). The correlation function is defined by  $C(n) = \chi_2^n$ , which can be written as

$$C(n) = \exp\left(-\frac{n}{n_c}\right), \quad n_c = -\frac{1}{\ln(|\chi_2|)}, \quad (35)$$

where  $n_c$  is the correlation step number. Thus, we define the dimensionless correlation length  $\lambda$  as

$$\lambda = \frac{n_c \ell}{r_c} \quad (36)$$

with  $\ell$  the spatial discretization of the correlated CTRW model. Note that the discretization length  $\ell$  should be smaller than the velocity correlation length,  $\lambda r_c$ .

Here we consider a simple transition matrix model, in which all diagonal entries are fixed to a constant  $a$ , and the remaining entries are equal to  $(1 - a)/(N - 1)$ ,

$$T_{ij} = a\delta_{ij} + \frac{1-a}{N-1}(1 - \delta_{ij}). \quad (37)$$

This transition matrix imposes the same correlation function for all starting velocities, and the diagonal value of  $a \leq 1$  determines the correlation strength. A value of  $a = 1$  implies perfect correlation, which renders the  $N$ -dimensional unity matrix,  $T_{ij} = \delta_{ij}$ . For  $a = 1/N$ , all transitions are equally probable, and the transition matrix is equal to the uniform matrix with  $T_{ij} = 1/N$ ; see Figure 5b. The transition matrix (37) has the eigenvalues  $\chi_1 = 1$  and

$$\chi_2 = \frac{Na - 1}{N - 1}, \quad (38)$$

such that we obtain for the dimensionless correlation length (36)

$$\lambda = \frac{\ell}{r_c \ln \left( \frac{N-1}{Na-1} \right)} \stackrel{N \gg 1}{\approx} \frac{\ell}{r_c \ln(a^{-1})}. \quad (39)$$

Thus, the correlation length  $\lambda$  is uniquely determined by the value of  $a$ .

For the steady state transition time distribution,  $\psi(\eta)$ , we use the truncated Pareto distribution,

$$\psi(\eta) = \frac{\beta \eta^{-1-\beta}}{\eta_\ell^{-\beta} - \eta_u^{-\beta}}, \quad \eta_\ell < \eta \leq \eta_u. \quad (40)$$

We fix the mean of the transition time distribution to 1, which ensures that the mean arrival time in the correlated CTRW model (25c) is equal to the one in the homogeneous model (25b). Note that one could also choose to scale the peak arrival time with that



of the homogeneous model, rather than fixing the mean arrival time. Furthermore we enforce a given ratio of  $r_\eta = \eta_u/\eta_\ell$  such that the power-law range covers the power-law regime observed in the breakthrough curves (see Figure 3). This determines  $\eta_\ell$  as

$$\eta_\ell = \frac{1-\beta}{\beta} \frac{1-r_\eta^{-\beta}}{r_\eta^{1-\beta}-1}. \quad (41)$$

This bounds the value of  $\eta_\ell$  between  $\ln(r_\eta)/(r_\eta-1)$ , which is the limit of (41) for  $\beta \rightarrow 0$ , and  $(r_\eta+1)/(2r_\eta)$ , which is the value of (41) for  $\beta = 2$ . For large contrasts  $r_\eta \gg 1$ ,  $\eta_\ell$  is approximately in  $(\ln(r)/r, 1/2]$ .

The transition time distribution (40) is illustrated in Figure 5. The slope  $\beta$  of the truncated Pareto distribution describes the heterogeneity of the velocity distribution. As  $\beta$  decreases, the transport becomes more anomalous because the probability of experiencing large transition times increases. Therefore, smaller  $\beta$  can be understood to represent higher flow heterogeneity, as is well known in the CTRW modeling framework [Berkowitz *et al.*, 2006].

In summary, the proposed transport model controls the velocity distribution and the velocity correlation with two independent parameters: the slope of the Pareto distribution,  $\beta$ , and the normalized correlation length  $\lambda$ .

#### 4.3.2. Simulation of convergent tracer tests

For the simulation of the convergent scenario, all the particles are injected at the injection well at  $r_0 = r_i$ , with  $r_i$  the radial distance between injection and pumping well. As discussed earlier, during the field tracer experiments, we flush the volume inside the packer with tracer-free fluid in order to ensure a sharp injection. Therefore, we use delta injection for both convergent and push-pull simulations. If the injection duration were

not short enough to be approximated as a delta function, the simulation could be easily adapted by continuously releasing particles during the injection time. The convergent BTCs are obtained by recording the particle travel times at the well radius  $r_w$  of the pumping well at a radial distance of  $r_c = r_i - r_w$ . The detailed procedure is:

1. Assign the desired values to  $k_v$ ,  $\alpha$ ,  $\beta$ ,  $\lambda$  and  $\ell$ .
2. Simulate the sequence of particle positions and times according to (25a) and (25c).
3. Sample particle arrival times at  $r_w$  and obtain the BTC.

### 4.3.3. Simulation of push-pull tracer tests

The implementation for the push-pull scenario is similar to the one for the convergent scenario. Here, particles are injected at  $r_0 = r_w$ , with  $r_w$  the radius of the injection well. Particles travel radially outwards until the push duration  $t_{\text{push}}$ . Then, the radial direction is reversed and particles travel back to the injection well until they reach the well radius  $r_w$ . The algorithmic steps are identical to those of the convergent test, except that step 2 is split into its “push” phase and the flow reversal “pull” phase.

## 5. Model behavior and field application

In this section, we study the model behavior of the proposed correlated CTRW model (25) depending on the three parameters  $\alpha$  (dispersivity),  $\beta$  (velocity distribution) and  $\lambda$  (velocity correlation). We then apply the model to the experimental data presented in Section 2 to explore the predictive capabilities of the model through the simultaneous prediction of BTCs in both convergent and push-pull tracer tests.

## 5.1. Model behavior

We first consider the dependence of the peak arrival time on dispersivity  $\alpha$ , the velocity distribution as parameterized by  $\beta$ , and the velocity correlation as parameterized by  $\lambda$ . Notice that the mean arrival time is the same in all cases because the model implementation detailed in the previous section forces the mean arrival of the correlated CTRW model (25c) to be equal to the one for the homogeneous CTRW model (25b). The minimum arrival time is obtained in the perfectly correlated CTRW, i.e.,  $a = 1$  in (37), which gives  $\lambda = \infty$ , and it is approximately

$$t_{\min} \approx \eta_{\ell} \frac{r_c^2}{2k_v}, \quad (42)$$

which can be obtained directly from (25c) by setting  $\eta_n \equiv \eta_{\ell}$ , the minimum non-dimensional transition time. For the perfectly correlated model, the minimum arrival time is at the same time the peak arrival. As  $\lambda$  decreases, the peak arrival time increases due to loss of flow coherence, as illustrated in Figure 6a.

The simple estimate (42) for the fully correlated case also indicates how the peak arrival depends on  $\beta$ . Recall that  $\eta_{\ell}$  depends on  $\beta$  as given in (41): it increases with increasing  $\beta$  up to a maximum of  $1/2$  for  $\beta = 2$ . From this, we conclude that the peak arrival time increases with increasing  $\beta$ , as illustrated in Figure 6. This may seem counter-intuitive at first. Notice however, that we force the mean of  $\psi(\eta)$  to be equal to 1 for a given range  $r_{\eta}$ . This means that as the probability of large transition times increases,  $\eta_{\ell}$  must decrease as  $\beta$  becomes smaller.

Finally, the dispersivity  $\alpha$  has essentially no impact on the peak arrival time, as illustrated in Figure 6b. This is intuitively clear when considering the mean arrival time (8)

for the homogeneous model, which at the same time is the peak arrival time. It is completely independent of  $\alpha$ , given that  $\alpha$  only impacts the spreading about the mean arrival time.

In Figure 7, we plot tracer BTCs for a set of random walk particle tracking simulations for the convergent and push-pull scenarios for various combinations of  $\alpha$ ,  $\beta$ , and  $\lambda$ . Different features of the BTCs are sensitive to variation in  $\alpha$  (dispersivity),  $\beta$  (velocity distribution) and  $\lambda$  (velocity correlation).

The dispersivity  $\alpha$  mainly impacts the early time behavior of the convergent BTCs. As expected, a decrease in  $\alpha$  leads to a slight decrease of the early arrivals due to the reduced particle dispersion (Figure 7a). Neither the late time tailing nor the peak position are affected by changes in  $\alpha$ . For the push-pull scenario, a decrease in  $\alpha$  decreases the relative dispersion of particle arrival times about the peak arrival times (Figure 7b). As for the push-pull test, the late-time scaling is not affected by the value of  $\alpha$ .

For fixed  $\lambda$ , an increase in  $\beta$  leads to a decrease in BTC tailing in both the convergent and push-pull scenarios, as expected in the CTRW modeling framework [Berkowitz *et al.*, 2006] (Figures 7c,d).

The correlation length  $\lambda$  impacts the early time BTC in the convergent scenario. We have already seen in Figure 6a that the peak arrival time increases with decreasing  $\lambda$ . Figure 7e shows that also the relative distance between the minimum arrival time and the peak arrival decreases with increasing  $\lambda$ . This behavior is caused by the fact that the particles sample a narrower window of the spectrum of transition times because of increased coherence. This leads to a decrease in the relative dispersion of early arrival times. For the push-pull scenario illustrated in Figure 7f, the impact of  $\lambda$  is more dramatic. The

relative spread of arrival times about the peak arrival time decreases for increasing  $\lambda$ , which reflects the partial reversibility of the transport process in the presence of velocity correlation. In the limit of a perfectly correlated scenario for  $\lambda = \infty$ , i.e.,  $a = 1$  in (37), the BTC is identical to the one for a homogeneous medium, which is fully characterized by the dispersivity  $\alpha$  (Figure 7f).

It is important to emphasize the difference between varying dispersivity  $\alpha$  and correlation length  $\lambda$ . While increasing  $\lambda$  and decreasing  $\alpha$  have qualitatively similar impacts on the relative early arrival times, their impacts on the BTC are very different. First, the peak arrival is essentially independent of dispersivity  $\alpha$ , but depends strongly on correlation  $\lambda$ . Secondly, the limit  $\lambda = \infty$  renders the BTC in the push-pull scenario identical to the one for a homogeneous medium because of full reversibility: no tailing is observed. For  $\alpha = 0$ , the strong BTC tailing in the push-pull scenario at long times remains unchanged.

## 5.2. Field application

We now test whether our CTRW model with correlated velocities is able to capture the transport behavior observed in the field, as evidenced by the BTC in the tracer tests. In particular, we address the central question of whether tracer tests under different flow configurations (convergent and push-pull tests) can be explained with *the same* set of model parameters.

We perform a comprehensive comparison between the measured BTCs and the simulated BTCs over the entire three-dimensional space of possible parameter values for dispersivity  $\alpha$ , velocity disorder  $\beta$ , and velocity correlation  $\lambda$ . We compute the unweighted mean square error (MSE), combined for the convergent and push-pull tests over the entire range of measured data for each test.

The MSE surfaces for each of the fracture planes (B1-2 and B1-4) are shown in Figure 8 over the  $\beta$ - $\lambda$  space, for a value of  $\alpha$  close to the optimum. These surfaces show the existence of a single minimum in the MSE surface, corresponding to the optimum choice of model parameters that best matches *both* the convergent test and the push-pull test. These values are:  $\alpha = 0.03$  [m],  $\beta = 0.75$  [-] and  $\lambda = 0.22$  [-] for fracture B1-2,  $\alpha = 0.02$  [m],  $\beta = 0.85$  [-] and  $\lambda = 0.06$  [-] for fracture B1-4.

A weighted MSE can also be applied to estimate the set of parameters [Chakraborty *et al.*, 2009]. This method utilizes the fact that concentration variance is proportional to concentration for the particle-tracking model. The estimated parameters with the weighted MSE gave very similar set of parameters with unweighted MSE.

This suggests that B1-2 has similar dispersivity ( $\alpha$ ), slightly higher velocity disorder (smaller  $\beta$ ), and significantly larger velocity correlation (larger  $\lambda$ ) than B1-4. One way to qualitatively (but independently) confirm this result is by comparing the characteristic fracture length in the field with the velocity correlation length inferred from our model. The estimated velocity correlation length from our model is  $\approx 1.32$  m for the B1-2 tracer test and  $\approx 0.36$  m for the B1-4 tracer test. Interestingly, this is of the same order of magnitude as the average distance between fracture connections measured independently by GPR imaging on the same site [Dorn *et al.*, 2012]. This would suggest that fracture flow velocities are well correlated along connections with other fractures, and that they de-correlate mainly when changing fracture planes. However, this hypothesis cannot be confirmed from this dataset alone.

The actual comparison between our model and the field data is shown in Figure 9. Our model accurately reproduces the BTCs of both push-pull and convergent tests (Fig-

ure 9(a),(b))—a quantitative agreement that is lost when neglecting velocity correlation (Figure 9(c),(d)). Therefore, our one-dimensional CTRW with one-step correlation in velocity is a parsimonious, yet accurate, approximation for describing macroscopic transport in fractured media.

Although the model results explain the field experiment data from our campaign, the model has some limitations. In our modeling framework, we intrinsically assumed that the velocity distribution for the field of interest can be represented by a single probability distribution. However, if the study field is non-stationary, this assumption should be revisited. We also assumed that regional flow was negligible compared to the flow induced by pumping rates used in the field experiments. In our case, ambient flow rates were estimated from point dilution experiments and found to be two orders of magnitude smaller than injection and pumping rates. However, if ambient flow were large enough to affect the tracer experiment, this would influence the reversibility of the flow [*Lesoff and Konikow*, 1997; *Altman et al.*, 2002]. If necessary, the modeling framework could be extended to incorporate non-stationarity and ambient flow.

## 6. Summary and Conclusions

In this paper, we have proposed a unified framework to characterize transport in fractured media and account for both velocity distribution and velocity correlation. We first presented results from convergent and push-pull tracer tests in fractured-granite at the Ploemeur subsurface observatory (H+ network, France). The field data suggest that velocity distribution and velocity correlation are the key controlling transport properties. In particular, the BTCs recorded in the field demonstrate the more reversible character of

tracer spreading for the push-pull test compared with the convergent test; an indication of the importance of velocity correlation.

Based on the field evidence, we have proposed a stochastic transport model that incorporates local dispersivity, Lagrangian velocity distribution, and Lagrangian velocity correlation as the three key transport processes, each characterized by a single parameter ( $\alpha$ ,  $\beta$  and  $\lambda$ , respectively). We have shown analytically that our model embodies other existing models of transport as particular cases: it is equivalent to the MRMT model under the assumption of negligible velocity correlation, and to the SCST model under the assumption of infinite correlation.

In contrast, our model is designed to capture the interplay between velocity distribution and velocity correlation, which we have illustrated with a sensitivity analysis of different metrics of the BTCs (early arrival time, peak arrival time, and late-time concentration decay) on the model parameters. The simplicity and versatility of our model has allowed us to perform a robust interpretation of the field tests, since the BTCs of both convergent and push-pull tests are retrieved accurately with the same set of parameters.

Our results raise important questions about modeling choices to simulate mixing and spreading in geologic media. For example, our model is designed to capture both push-pull and convergent BTCs with scale-independent local dispersivity, in contrast with the traditional ansatz of a dispersivity that increases with the observational scale [*Gelhar et al.*, 1992]. Because our model accounts for macroscopic features with  $\lambda$  and  $\beta$ , it may permit removing the (spurious) scale dependence of local dispersivity  $\alpha$ .

Finally, because our model distinguishes between the spreading caused by advective processes ( $\lambda$ ) and diffusive processes ( $\alpha$ ), we conjecture that it may provide an avenue to



model not only tracer spreading but also fluid mixing [*Le Borgne et al.*, 2010, 2011; *Dentz et al.*, 2011b; *Jha et al.*, 2011; *de Dreuzy et al.*, 2012b; *Chiogna et al.*, 2012; *Jha et al.*, 2013]. The prediction of mixing and spreading rates in field-scale experiments remains, however, an exciting open question.

**Acknowledgments.** The authors thank Nicolas Lavenant and Rebecca Hochreutener for their help in setting up and running the field experiments. Our experimental data can be accessed at <http://hplus.ore.fr/en>. Funding for this work was provided by the INTERREG IV project CLIMAWAT, the national network of hydrogeological sites H+ ([hplus.ore.fr](http://hplus.ore.fr)). MD acknowledges the support of the European Research Council (ERC) through the project MHetScale (617511). RJ acknowledges the support of the US Department of Energy (grant DE-SC0003907), and a MISTI Global Seed Funds award.

## References

- Altman, S. J., L. C. Meigs, T. L. Jones, and S. A. McKenna (2002), Controls of mass recovery rates in single-well injection-withdrawal tracer tests with a single-porosity, heterogeneous conceptualization, *Water Resour. Res.*, *38*(7), 30–1–30–15.
- Becker, M. W., and A. M. Shapiro (2000), Tracer transport in fractured crystalline rock: Evidence of nondiffusive breakthrough tailing, *Water Resour. Res.*, *36*(7), 1677–1686.
- Becker, M. W., and A. M. Shapiro (2003), Interpreting tracer breakthrough tailing from different forced-gradient tracer experiment configurations in fractured bedrock, *Water Resour. Res.*, *39*, 1024.
- Benke, R., and S. Painter (2003), Modeling conservative tracer transport in fracture networks with a hybrid approach based on the Boltzmann transport equation, *Water Re-*

*sour. Res.*, *39*, 1324.

Benson, D. A., and M. M. Meerschaert (2009), A simple and efficient random walk solution of multi-rate mobile/immobile mass transport equations, *Adv. Water Resour.*, *32*, 532–539.

Benson, D. A., S. W. Wheatcraft, and M. M. Meerschaert (2000), Application of a fractional advection-dispersion equation, *Water Resour. Res.*, *36*, 1403–1412.

Berkowitz, B., and H. Scher (1997), Anomalous transport in random fracture networks, *Phys. Rev. Lett.*, *79*(20), 4038–4041.

Berkowitz, B., A. Cortis, M. Dentz, and H. Scher (2006), Modeling non-Fickian transport in geological formations as a continuous time random walk, *Rev. Geophys.*, *44*(2), RG2003.

Bibby, R. (1981), Mass transport of solutes in dual-porosity media, *Water Resour. Res.*, *17*(4), 1075–1081.

Bijeljic, B., and M. J. Blunt (2006), Pore-scale modeling and continuous time random walk analysis of dispersion in porous media, *Water Resour. Res.*, *42*, W01,202.

Bodvarsson, G. S., W. B., R. Patterson, and D. Williams (1999), Overview of scientific investigations at Yucca Mountain: the potential repository for high-level nuclear waste, *J. Contam. Hydrol.*, *38*, 3–24.

Brouyère, S., J. Batlle-Aguilar, P. Goderniaux, and A. Dassargues (2008), A new tracer technique for monitoring groundwater fluxes: The finite volume point dilution method, *J. Contam. Hydrol.*, *95*(3), 121–140.

Brown, S., A. Caprihan, and R. Hardy (1998), Experimental observation of fluid flow channels in a single fracture, *J. Geophys. Res.*, *103*(B3), 5125–5132.

- 614 Cacas, M. C., E. Ledoux, G. de Marsily, A. Barbreau, P. Calmels, B. Gaillard, and  
 615 R. Margritta (1990), Modeling fracture flow with a stochastic discrete fracture network:  
 616 calibration and validation. 2. The transport model, *Water Resour. Res.*, *26*(3), 491–500.
- 617 Carrera, J., X. Sánchez-Vila, I. Benet, A. Medina, G. A. Galarza, and J. Guimerá (1998),  
 618 On matrix diffusion: formulations, solution methods and qualitative effects, *Hydrogeol.*  
 619 *J.*, *6*, 178–190.
- 620 Chakraborty, P., M. M. Meerschaert, and C. Y. Lim (2009), Parameter estimation for frac-  
 621 tional transport: A particle-tracking approach, *Water Resour. Res.*, *45*(10), W10,415.
- 622 Chiogna, G., D. L. Hochstetler, A. Bellin, P. K. Kitanidis, and M. Rolle (2012), Mixing,  
 623 entropy and reactive solute transport, *Geophys. Res. Lett.*, *39*, L20,405.
- 624 Cirpka, O. A., and P. K. Kitanidis (2000), An advective-dispersive streamtube approach  
 625 for the transfer of conservative tracer data to reactive transport, *Water Resour. Res.*,  
 626 *36*, 1209–1220.
- 627 Cueto-Felgueroso, L., and R. Juanes (2013), Forecasting long-term gas production from  
 628 shale, *Proc. Natl. Acad. Sci. U.S.A.*, *110*(49), 19,660–19,661.
- 629 Curtis, J. B. (2002), Fractured shale-gas systems, *AAPG Bull.*, *86*, 1921–1938.
- 630 Dagan, G., and E. Bressler (1979), Solute dispersion in unsaturated soil at field scale, I,  
 631 Theory, *Soil Sci. Soc. Am. J.*, *43*, 461–466.
- 632 de Anna, P., T. Le Borgne, M. Dentz, A. M. Tartakovsky, D. Bolster, and P. Davy (2013),  
 633 Flow intermittency, dispersion, and correlated continuous time random walks in porous  
 634 media, *Phys. Rev. Lett.*, *110*, 184,502.
- 635 de Dreuzy, J. R., P. Davy, and O. Bour (2001), Hydraulic properties of two-dimensional  
 636 random fracture networks following a power law length distribution: 1. Effective con-

- nectivity, *Water Resour. Res.*, *37*(8), 2065–2078.
- de Dreuzy, J. R., J. Bodin, H. L. Grand, P. Davy, D. Boulanger, A. Battais, O. Bour, P. Gouze, and G. Porel (2006), General database for ground water site information, *Groundwater*, *44*(5), 743–748.
- de Dreuzy, J. R., Y. Méheust, and G. Pichot (2012a), Influence of fracture scale heterogeneity on the flow properties of three-dimensional discrete fracture networks (DFN), *J. Geophys. Res.*, *117*, B11,207.
- de Dreuzy, J. R., J. Carrera, M. Dentz, and T. Le Borgne (2012b), Time evolution of mixing in heterogeneous porous media, *Water Resour. Res.*, *48*, W06,511.
- Dentz, M., and B. Berkowitz (2003), Transport behavior of a passive solute in continuous time random walks and multirate mass transfer, *Water Resour. Res.*, *39*, 1111.
- Dentz, M., and D. Bolster (2010), Distribution- versus correlation-induced anomalous transport in quenched random velocity fields, *Phys. Rev. Lett.*, *105*, 244,301.
- Dentz, M., D. Bolster, and T. Le Borgne (2009), Concentration statistics for transport in random media, *Phys. Rev. E*, *80*, 010,101(R).
- Dentz, M., P. Gouze, and J. Carrera (2011a), Effective non-local reaction kinetics for transport in physically and chemically heterogeneous media, *J. Contam. Hydrol.*, *120–121*, 222–236.
- Dentz, M., T. Le Borgne, A. Englert, and B. Bijeljic (2011b), Mixing, spreading and reaction in heterogeneous media: A brief review, *J. Contam. Hydrol.*, *120–121*, 1–17.
- Dorn, C., N. Linde, T. Le Borgne, O. Bour, and M. Klepikova (2012), Inferring transport characteristics in a fractured rock aquifer by combining single-hole ground-penetrating radar reflection monitoring and tracer test data, *Water Resour. Res.*, *48*, W11,521.

- 660 Dorn, C., N. Linde, T. Le Borgne, O. Bour, and J.-R. de Dreuzy (2013), Conditioning  
 661 of stochastic 3-D fracture networks to hydrological and geophysical data, *Adv. Water*  
 662 *Resour.*, *62*, 79–89.
- 663 Feenstra, S., J. A. Cherry, and E. A. Sudicky (1985), Matrix diffusion effects on contam-  
 664 inant migration from an injection well in fractured sandstone, *Ground Water*, *22*(3),  
 665 307–316.
- 666 Geiger, S., A. Cortis, and J. T. Birkholzer (2010), Upscaling solute transport in naturally  
 667 fractured porous media with the continuous time random walk method, *Water Resour.*  
 668 *Res.*, *46*, W12,530.
- 669 Gelhar, L. W., C. Welty, and K. R. Rehfeldt (1992), A critical review of data on field-scale  
 670 dispersion in aquifers, *Water Resour. Res.*, *28*, 1955–1974.
- 671 Gerke, H. H., and M. T. van Genuchten (1993), A dual-porosity model for simulating the  
 672 preferential flow of water and solutes in structured porous media, *Water Resour. Res.*,  
 673 *29*(2), 305–319.
- 674 Ginn, T. R. (2001), Stochastic-convective transport with nonlinear reactions and mixing:  
 675 finite streamtube ensemble formulation for multicomponent reaction systems with intra-  
 676 streamtube dispersion, *J. Contam. Hydrol.*, *47*, 1–28.
- 677 Haggerty, R., and S. M. Gorelick (1995), Multiple-rate mass transfer for modeling diffusion  
 678 and surface reactions in media with pore-scale heterogeneity, *Water Resour. Res.*, *31*,  
 679 2383–2400.
- 680 Haggerty, R., S. W. Fleming, L. C. Meigs, and S. A. McKenna (2001), Tracer tests in a  
 681 fractured dolomite 2. Analysis of mass transfer in single-well injection-withdrawal tests,  
 682 *Water Resour. Res.*, *37*, 1129–1142.

Harvey, C. F., and S. M. Gorelick (1995), Temporal moment-generating equations: Modeling transport and mass transfer in heterogeneous aquifers, *Water Resour. Res.*, *31*, 1895–1911.

Huyakorn, P. S., S. Panday, and Y. S. Wu (1994), A three-dimensional multiphase flow model for assessing NAPL contamination in porous and fractured media, 1. Formulation, *J. Contam. Hydrol.*, *16*, 109.

Jha, B., L. Cueto-Felgueroso, and R. Juanes (2011), Fluid mixing from viscous fingering, *Phys. Rev. Lett.*, *106*, 194,502.

Jha, B., L. Cueto-Felgueroso, and R. Juanes (2013), Synergetic fluid mixing from viscous fingering and alternating injection, *Phys. Rev. Lett.*, *111*, 144,501.

Juanes, R., J. Samper, and J. Molinero (2002), A general and efficient formulation of fractures and boundary conditions in the finite element method, *Int. J. Numer. Meth. Engrg.*, *54*(12), 1751–1774.

Kang, P. K., M. Dentz, T. Le Borgne, and R. Juanes (2011a), Spatial Markov model of anomalous transport through random lattice networks, *Phys. Rev. Lett.*, *107*, 180,602, doi:10.1103/PhysRevLett.107.180,602.

Kang, P. K., M. Dentz, and R. Juanes (2011b), Predictability of anomalous transport on lattice networks with quenched disorder, *Phys. Rev. E*, *83*, 030,101(R).

Kang, P. K., P. de Anna, J. P. Nunes, B. Bijeljic, M. J. Blunt, and R. Juanes (2014), Pore-scale intermittent velocity structure underpinning anomalous transport through 3D porous media, *Geophys. Res. Lett.*, *41*, 1–7, doi:10.1002/2014GL061,475.

Karimi-Fard, M., L. J. Durlofsky, and K. Aziz (2004), An efficient discrete fracture model applicable for general purpose reservoir simulators, *Soc. Pet. Eng. J.*, *9*(2), 227–236.

- 706 Kazemi, H., L. S. Merrill, K. L. Porterfield, and P. R. Zeman (1976), Numerical simulation  
707 of water-oil flow in naturally fractured reservoirs, *Soc. Pet. Eng. J.*, *16*(6), 317–326.
- 708 Kerner, B. S. (1998), Experimental features of self-organization in traffic flow, *Phys. Rev.*  
709 *Lett.*, *81*(17), 3797–3800.
- 710 Kiraly, L. (1979), Remarques sur la simulation des failles et du réseau karstique par  
711 éléments finis dans les modèles d’écoulement, *Bull. Centre Hydrogéol.*, *3*, 155–167, Univ.  
712 of Neuchâtel, Switzerland.
- 713 Le Borgne, T., and P. Gouze (2008), Non-Fickian dispersion in porous media: 2. Model  
714 validation from measurements at different scales, *Water Resour. Res.*, *44*, W06,427.
- 715 Le Borgne, T., O. Bour, M. Riley, P. Gouze, P. Pezard, A. Belghoul, R. L. P. G. Lods and,  
716 R. B. Greswell, P. A. Ellis, E. Isakov, and B. J. Last (2007), Comparison of alternative  
717 methodologies for identifying and characterizing preferential flow paths in heterogeneous  
718 aquifers, *J. Hydrol.*, *345*, 134–148.
- 719 Le Borgne, T., M. Dentz, and J. Carrera (2008), Lagrangian statistical model for transport  
720 in highly heterogeneous velocity fields, *Phys. Rev. Lett.*, *101*, 090,601.
- 721 Le Borgne, T., M. Dentz, D. Bolster, J. Carrera, J.-R. de Dreuzy, and P. Davy (2010),  
722 Non-Fickian mixing: Temporal evolution of the scalar dissipation rate in heterogeneous  
723 porous media, *Adv. Water Resour.*, *33*(12), 1468–1475.
- 724 Le Borgne, T., M. Dentz, P. Davy, D. Bolster, J. Carrera, J.-R. de Dreuzy, and O. Bour  
725 (2011), Persistence of incomplete mixing: A key to anomalous transport, *Phys. Rev. E*,  
726 *84*, 015,301(R).
- 727 Lessoff, S. C., and L. F. Konikow (1997), Ambiguity in measuring matrix diffusion with  
728 single-well injection/recovery tracer tests, *Groundwater*, *35*(1), 166–176.

Maloszewski, P., and A. Zuber (1985), On the theory of tracer experiments in fissured rocks with a porous matrix, *J. Hydrol.*, 79(3–4), 333–358.

Martinez-Landa, L., and J. Carrera (2005), An analysis of hydraulic conductivity scale effects in granite (Full-scale Engineered Barrier Experiment (FEBEX), Grimsel, Switzerland), *Water Resour. Res.*, 41(3), W03,006.

Martinez-Landa, L., J. Carrera, M. Dentz, D. Fernandez-Garcia, A. Nardi, and M. W. Saaltink (2012), Mixing induced reactive transport in fractured crystalline rocks, *Appl. Geochem.*, 27(2), 479–489.

McKenna, S. A., L. C. Meigs, and R. Haggerty (2001), Tracer tests in a fractured dolomite 3. Double-porosity, multiple-rate mass transfer processes in convergent flow tracer tests, *Water Resour. Res.*, 37, 1143–1154.

Méheust, Y., and J. Schmittbuhl (2000), Flow enhancement of a rough fracture, *Geophys. Res. Lett.*, 27(18), 2989–2992.

Moench, A. F. (1995), Convergent radial dispersion in a double-porosity aquifer with fracture skin: analytical solution and application to a field experiment in fractured chalk, *Water Resour. Res.*, 31(8), 1823–1835.

Molinero, J., and J. Samper (2006), Large-scale modeling of reactive solute transport in fracture zones of granitic bedrocks, *J. Contam. Hydrol.*, 82, 293–318.

Molinero, J., J. Samper, and R. Juanes (2002), Numerical modeling of the transient hydrogeological response produced by tunnel construction in fractured bedrocks, *Eng. Geol.*, 64(4), 369–386.

Moreno, L., and I. Neretnieks (1993), Fluid flow and solute transport in a network of channels, *J. Contam. Hydrol.*, 14, 163–194.



- 752 Neretnieks, I. (1983), A note on fracture flow dispersion mechanisms in the ground, *Water*  
 753 *Resour. Res.*, *19*(2), 364–370.
- 754 Neuman, S. P., C. L. Winter, and C. M. Newman (1987), Stochastic theory of field-scale  
 755 Fickian dispersion in anisotropic porous media, *Water Resour. Res.*, *23*(3), 453–466.
- 756 Nicolaides, C., L. Cueto-Felgueroso, M. C. Gonzalez, and R. Juanes (2012), A metric of  
 757 influential spreading during contagion dynamics through the air transportation network,  
 758 *PLoS ONE*, *7*(7), e40,961.
- 759 Nordqvist, A. W., Y. W. Tsang, C. F. Tsang, B. Dverstorp, and J. Andersson (1992),  
 760 A variable aperture fracture network model for flow and transport in fractured rocks,  
 761 *Water Resour. Res.*, *28*(6), 1703–1713.
- 762 Pruess, K. (2006), Enhanced geothermal systems (EGS) using CO<sub>2</sub> as working fluid: novel  
 763 approach for generating renewable energy with simultaneous sequestration of carbon,  
 764 *Geothermics*, *35*, 351–367.
- 765 Reimus, P. W., and T. J. Callahan (2007), Matrix diffusion rates in fractured volcanic  
 766 rocks at the Nevada Test Site: Evidence for a dominant influence of effective fracture  
 767 apertures, *Water Resour. Res.*, *43*, W07,421.
- 768 Rinaldo, A., et al. (2012), Reassessment of the 2010-2011 Haiti cholera outbreak and  
 769 rainfall-driven multiseason projections, *Proc. Natl. Acad. Sci. U.S.A.*, *109*(17), 6602–  
 770 6607.
- 771 Risken, H. (1989), *The Fokker–Planck Equation*, Springer, Berlin.
- 772 Ruelleu, S., F. Moreau, O. Bour, D. Gapais, and G. Martelet (2010), Impact of gen-  
 773 tly dipping discontinuities on basement aquifer recharge: An example from Ploemeur  
 774 (Brittany, France), *J. Appl. Geophys.*, *70*(2), 161–168.

- Schmid, K. S., S. Geiger, and K. S. Sorbie (2013), Higher order FE–FV method on unstructured grids for transport and two-phase flow with variable viscosity in heterogeneous porous media, *J. Comput. Phys.*, *241*, 416–444.
- Schumer, R., D. A. Benson, M. M. Meerschaert, and B. Baeumer (2003), Fractal mobile/immobile solute transport, *Water Resour. Res.*, *39*, 1022.
- Smart, P. L., and I. M. S. Laidlaw (1977), An evaluation of some fluorescent dyes for water tracing, *Water Resour. Res.*, *13*(1), 15–33.
- Szulczewski, M. L., C. W. MacMinn, H. J. Herzog, and R. Juanes (2012), Lifetime of carbon capture and storage as a climate-change mitigation technology, *Proc. Natl. Acad. Sci. U.S.A.*, *109*(14), 5185–5189.
- Tsang, Y. W. (1992), Usage of “equivalent apertures” for rock fractures as derived from hydraulic and tracer tests, *Water Resour. Res.*, *28*(5), 1451–1455.
- Tsang, Y. W. (1995), Study of alternative tracer tests in characterizing transport in fractured rocks, *Geophys. Res. Lett.*, *22*, 1421–1424.
- Tsang, Y. W., C. F. Tsang, I. Neretnieks, and L. Moreno (1988), Flow and tracer transport in fractured media: A variable aperture channel model and its properties, *Water Resour. Res.*, *24*(12), 2049–2060.
- Tsang, Y. W., C. F. Tsang, F. V. Hale, and B. Dverstorp (1996), Tracer transport in a stochastic continuum model of fractured media, *Water Resour. Res.*, *32*(10), 3077–3092.
- Wilking, J. N., V. Zaburdaev, M. D. Volder, R. Losick, M. P. Brenner, and D. A. Weitz (2013), Liquid transport facilitated by channels in *Bacillus subtilis* biofilms, *Proc. Natl. Acad. Sci. U.S.A.*, *110*(3), 848–852.

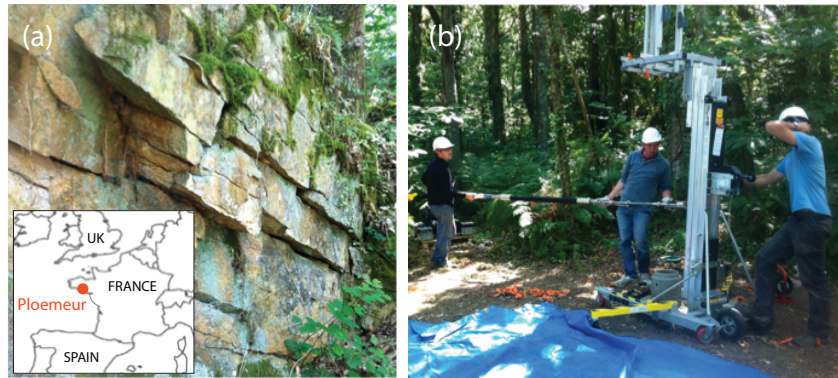


**Figure 1.** (a) Outcrop of fractured granite at the Ploemur field site. Inset: map showing the location of Ploemur, France. (b) Photo from the installation of double packer system in B1 borehole.

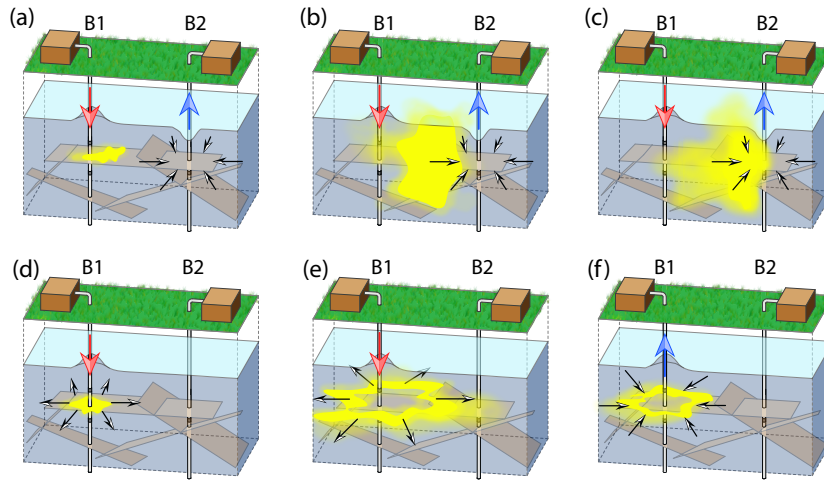


**Figure 2.** Schematic of the tracer tests conducted. (a,b,c) Convergent test with tracer placement at borehole B1 and pumping from borehole B2. Two different fracture planes at different depths (B1-2 and B1-4) are used for two separate tests. (d,e,f) Push-pull test from borehole B1. The same two fracture planes (B1-2 and B1-4) are used.

**Table 1.** Details of the conditions and parameters of the four tracer experiments.

Experimental parameters	Experiments			
	B1-2 convergent	B1-2 push-pull	B1-4 convergent	B1-4 push-pull
Tracer injection fracture	B1-2	B1-2	B1-4	B1-4
Withdrawal borehole / fracture	B2	B1-2	B2	B1-4
Flow configuration	convergent	push-pull	convergent	push-pull
Tracer injection depth	50.5 m	50.5 m	78.7 m	78.7 m
Packer system at B1	double packer	double packer	double packer	double packer
Packer system at B2	single packer	single packer	single packer	single packer
Injection rate	1 L/min	6 L/min	1 L/min	5 L/min
Injection duration	15 min	30 min	15 min	80 min
Withdrawal rate	120 L/min	6 L/min	100 L/min	5 L/min
Injected mass	5 g	0.1 g	1.5 g	0.4 g
Peak arrival time	30 min	57 min	35 min	140 min
Peak concentration	590 ppb	353 ppb	312 ppb	690 ppb
Mass recovery	96 %	89 %	99 %	87 %
Late-time tailing slope	$\sim 1.7$		$\sim 1.85$	

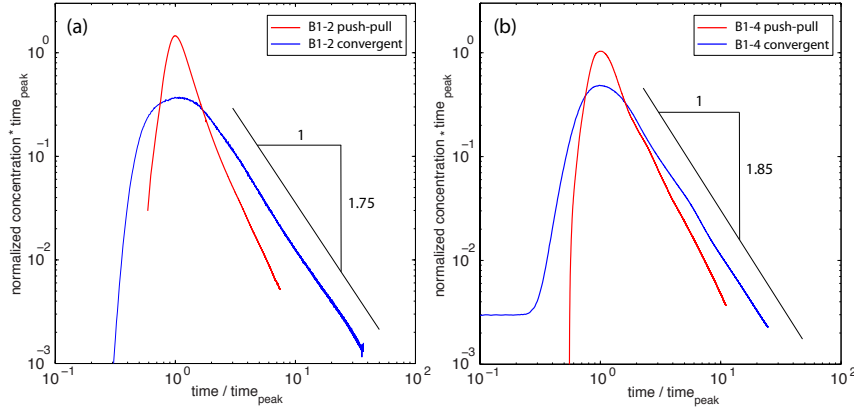


**Figure 3.** Measured breakthrough curves (BTC) for the tracer tests we conducted, in the form of a normalized time (peak arrival at dimensionless time of 1) and normalized concentration (such that the area under the BTC is identically equal to 1). The tracer concentration is measured every 20 seconds. (a) BTCs for fracture plane B1-2. (b) BTCs for fracture plane B1-4.

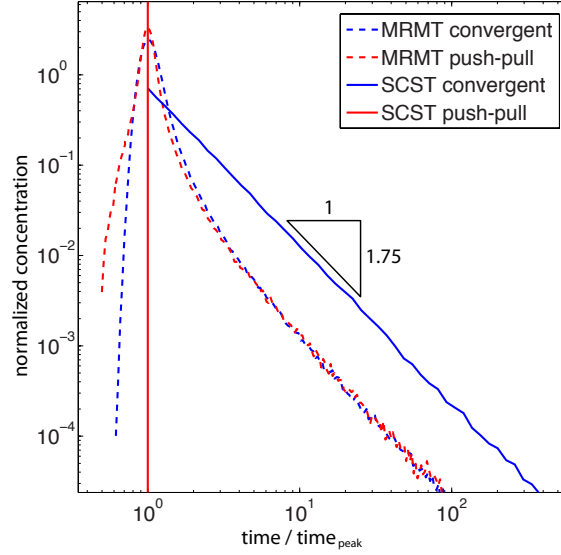


**Figure 4.** Comparison of the breakthrough curves (BTC) for the MRMT and SCST models characterized by the distributions (21) and (22) with  $\beta = 1.75$ ,  $\eta_0 = 0.005$  and  $k_0 = 200$ , respectively. The BTCs for the convergent and push-pull scenarios are almost identical in the MRMT approach because solute spreading is irreversible. In contrast, the BTC for the convergent and push-pull scenarios in the SCST model are drastically different: in the absence of local dispersion, the BTC in the push-pull scenario is a delta distribution due to the perfect velocity correlation within each streamtube, i.e., full reversibility.

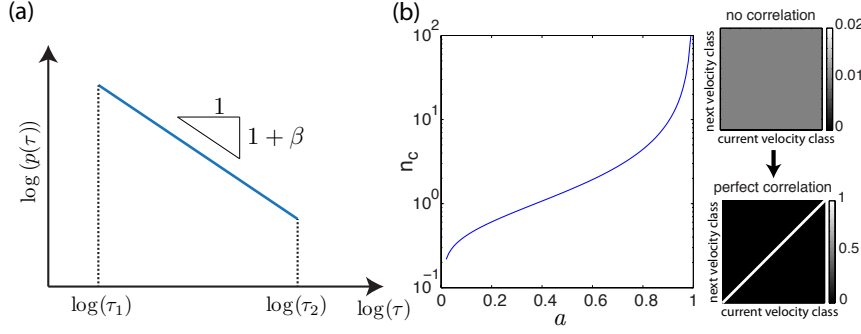


**Figure 5.** Key transport characteristics of our proposed CTRW model. (a)  $\psi(\eta)$  follows the truncated Pareto distribution (40). The slope of the power law,  $\beta$ , characterizes the velocity heterogeneity of the fractured medium. As  $\beta$  decreases, the velocity heterogeneity increases. (b) Number  $n_c$  of correlation steps given by (35) as a function of parameter  $a$  for  $N = 100$  velocity classes. By changing the value of the diagonal,  $a$ , we can systematically vary the strength of the velocity correlation from the uniform transition matrix that is equivalent to the uncorrelated velocity field to the identity matrix that represents a fully correlated velocity field.



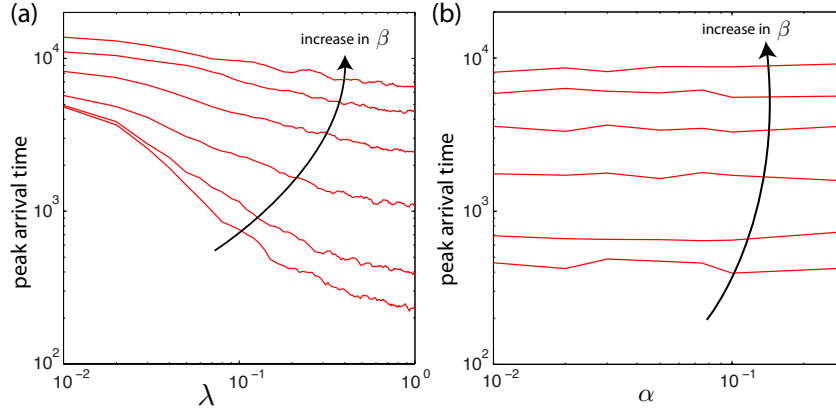


**Figure 6.** Sensitivity analysis for the peak arrival time on the three parameters of our CTRW model. (a) Change in peak arrival times for  $\alpha = 0.3$  with varying  $\lambda$ . Different curves represent different degrees of velocity heterogeneity ( $\beta = 0.5, 0.6, 0.8, 1, 1.2, 1.4$ ). (b) Change in peak arrival times for  $\lambda = 0.2$  with varying  $\alpha$ . Different curves represent different  $\beta = 0.5, 0.6, 0.8, 1, 1.2, 1.4$ .

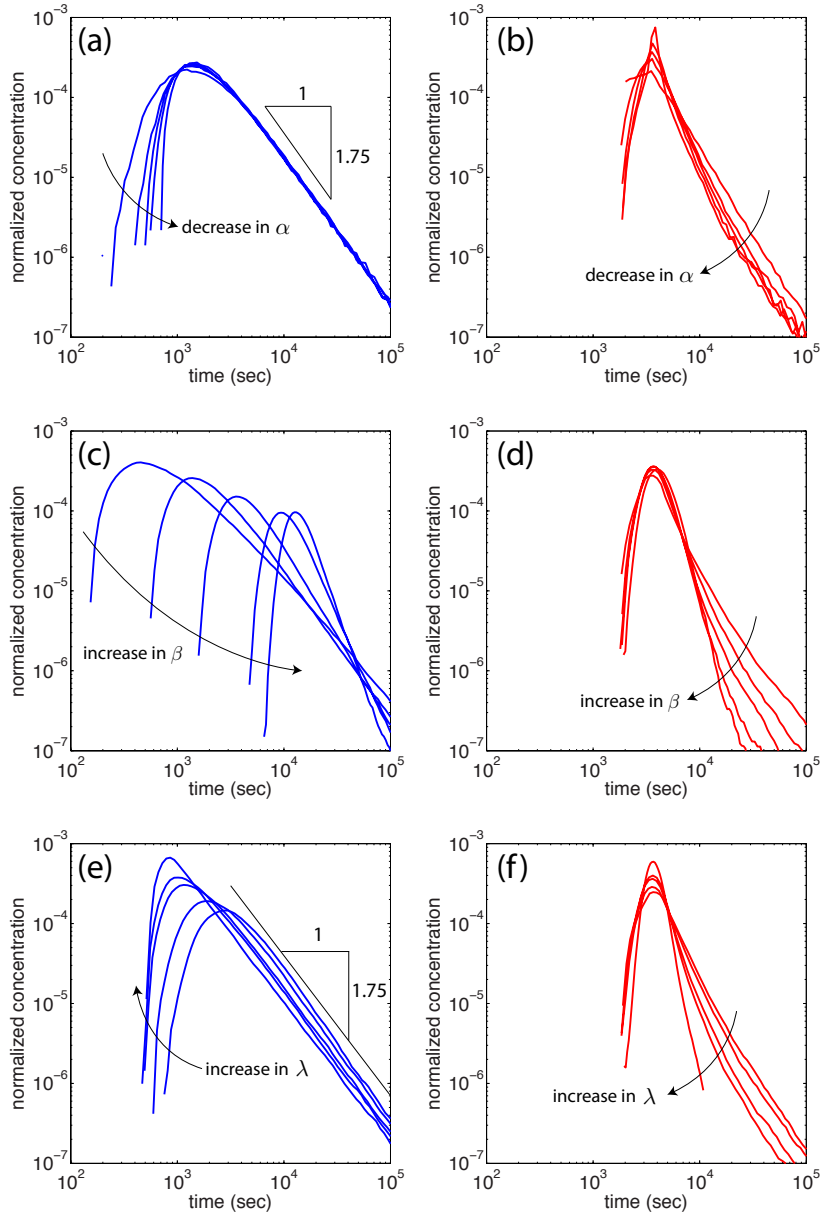


**Figure 7.** Impact of parameters  $\alpha$ ,  $\beta$  and  $\lambda$  of our CTRW model on transport behavior. Left (a,c,e): convergent tests. Right (b,d,f): push-pull tests. Top (a,b): impact of dispersivity ( $\alpha = 0, 0.02, 0.05, 0.1, 0.3$ ) for fixed  $\beta = 0.75$  and  $\lambda = 0.2$ . Middle (c,d): impact of velocity distribution ( $\beta = 0.5, 0.75, 1, 1.5, 2$ ) for fixed value of  $\alpha = 0.03$  and  $\lambda = 0.2$ . Bottom (e,f): impact of velocity correlation ( $\lambda = 0.05, 0.1, 0.3, 0.5, \infty$ ) for fixed value of  $\alpha = 0.03$  and  $\beta = 0.75$ .

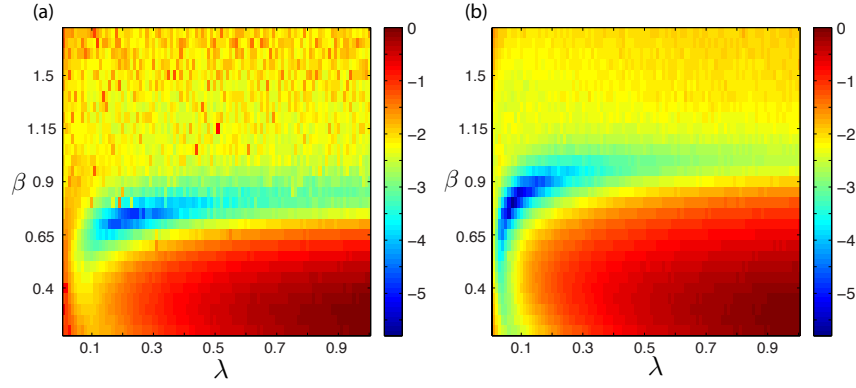


**Figure 8.** Plot of the mean square error (MSE) between modeled and measured BTCs for different model parameters. The error is for the combined differences of the convergent and push-pull tests. (a) MSE for the B1-2 fracture with a value  $\alpha = 0.03$ . The global minimum is for  $\alpha = 0.03$ ,  $\beta = 0.75$  and  $\lambda = 0.22$ . (b) MSE for the B1-4 fracture with a value  $\alpha = 0.02$ . The global minimum is for  $\alpha = 0.02$ ,  $\beta = 0.85$  and  $\lambda = 0.06$ .

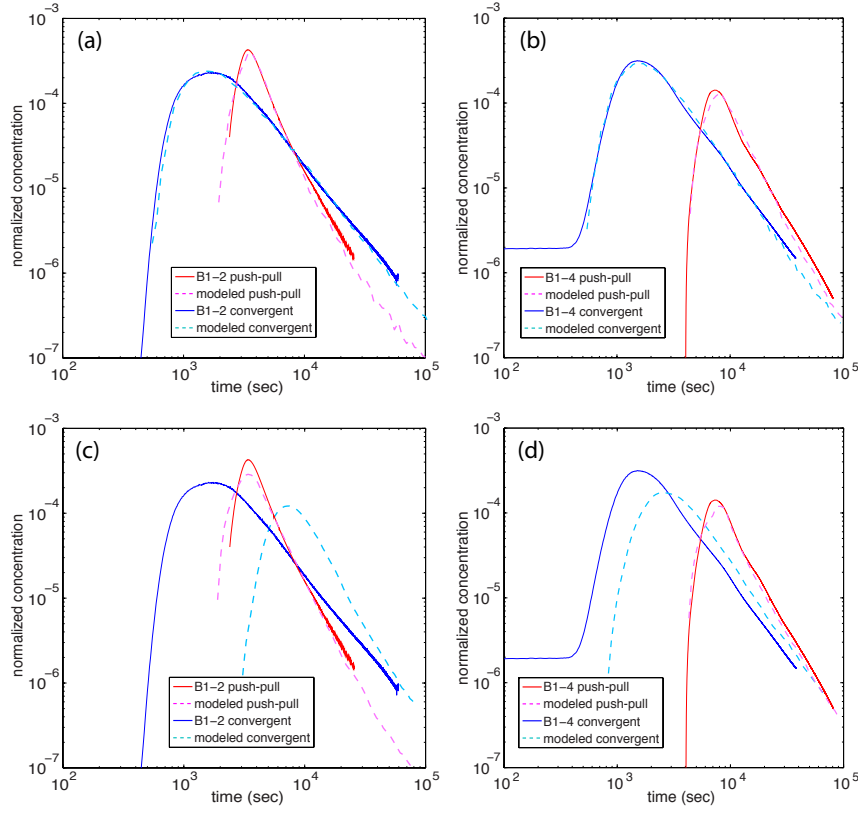


**Figure 9.** Comparison of measured and modeled BTCs for both convergent and push-pull tests, modeled with the same set of parameters. (a) B1-2 fracture; correlated CTRW model with parameters  $\alpha = 0.03$ ,  $\beta = 0.75$ , and  $\lambda = 0.22$ . (b) B1-4 fracture; correlated CTRW model with parameters  $\alpha = 0.02$ ,  $\beta = 0.85$ , and  $\lambda = 0.06$ . (c) B1-2 fracture; uncorrelated CTRW model with parameters  $\alpha = 0.03$ ,  $\beta = 0.95$ , and  $\lambda = 0$ . (d) B1-4 fracture; uncorrelated CTRW model with parameters  $\alpha = 0.02$ ,  $\beta = 0.65$ , and  $\lambda = 0$ .